

Synthesis of various morphologies of CoFe bimetallic hydroxides for enhanced OER performance

Liming Yang¹⁾, Yuanbo Cao¹⁾, Linsong Wang¹⁾, Tao Yang^{1,2),}✉, Kang Wang¹⁾, Enhui Wang^{1,2)}, Xiangtao Yu¹⁾, Hongyang Wang^{3),}✉, Kuo-Chih Chou¹⁾ and Xinmei Hou^{1,2,4),}✉

1) Institute for Carbon Neutrality, University of Science and Technology Beijing, Beijing 100083, China

2) Institute of Steel Sustainable Technology, Liaoning Academy of Materials, Shenyang 110000, China

3) State Key Laboratory of Environmental Criteria and Risk Assessment, Chinese Research Academy of Environmental Sciences, Beijing 100012, China

4) Beijing Advanced Innovation Center for Materials Genome Engineering, University of Science and Technology Beijing, Beijing 100083, China

✉Corresponding authors: Tao Yang E-mail: yangtaoustb@ustb.edu.cn;
Hongyang Wang E-mail: wanghongyang_why@126.com; Xinmei Hou E-mail: houxinmeiustb@ustb.edu.cn

Abstract: CoFe bimetallic hydroxides (CoFe BMHs) are widely used as excellent catalysts in the field of water splitting. However, the influence of morphologies of CoFe BMHs on catalyst performance has not been systematically studied. In this study, we prepared CoFe BMHs nano-flowers (CoFe BMHs NFs), CoFe BMHs nano-sheets (CoFe BMHs NSHs), CoFe BMHs nano-rods (CoFe BMHs NRs), and CoFe BMHs nano-spheres (CoFe BMHs NSPs) on nickel foam using a hydrothermal method. Among them, CoFe BMHs NSHs exhibited the most beneficial catalytic

activity. At a current density of 100 mA cm^{-2} , the overpotential for oxygen evolution reaction (OER) was 282 mV, and the overall water splitting voltage was 1.923 V. The C_{dl} value of CoFe BMHs NSHs is the largest in CoFe BMHs, which proves that CoFe BMHs NSHs have the largest active area. Furthermore, the active site in the OER process was found to be MOOH by in situ Raman characterization and the generation of the active substance is an irreversible process. This work provides significant insights into the design of catalyst morphologies, offering valuable guidelines for enhancing the performance of other catalysts.

Keywords: CoFe Bimetallic Hydroxides, Various Morphologies, Hydrogen Evolution Reaction, Oxygen Evolution Reaction, Overall Water Splitting

Accepted Manuscript Not Certified

1. Introduction

Hydrogen energy, as a clean energy source, can significantly reduce greenhouse gas emissions and play a crucial role in combating climate change [1-3]. Among various hydrogen production methods, water splitting is considered the most environmentally friendly approach [4]. In the process of overall water splitting, the four-electron process of anode OER is slow and consumes most of the energy input, which determines the energy consumption of the entire reaction [5-6]. Although precious metal catalysts (e.g., $\text{IrO}_2/\text{RuO}_2$) exhibit excellent activity in OER [7-8], they are costly. Currently, large-scale electrolyzers in industrial settings mainly utilize nickel-based catalysts, such as pure nickel mesh or nickel foam, which possess excellent conductivity, high-volume porosity, and good mechanical properties. However, it is challenging to further increase the number of catalytic sites solely through structural optimization of nickel mesh or foam. Optimization can be performed at a more microscopic scale, such as depositing catalysts with higher specific surface area and catalytic activity on substrates [9-12].

Transition metal hydroxides are well-known electrocatalysts due to their easy-to-obtain raw materials, adjustable chemical composition, superior activity, and stability [13-15]. Among them, CoFe bimetallic hydroxides (CoFe BMHs) exhibit excellent OER performance under alkaline conditions [16-18]. However, the low electrical conductivity of CoFe BMHs hinders the expression of catalytic activity [19]. Growing CoFe BMHs on a nickel foam substrate is an effective method to address this issue [20-21]. Additionally, the microstructural morphology of the catalyst also influences the active sites and intrinsic activity. Although researchers have prepared CoFe BMHs nano-flowers (CoFe BMHs NFs) [22-23], CoFe BMHs nano-sheets (CoFe BMHs NSHs) [24-25], and CoFe BMHs nanorods (CoFe BMHs NRs) [26], using various methods, there has been no systematic study on the relationship between the morphology preparation of CoFe BMHs and their catalytic performance.

Herein, we utilized a one-step hydrothermal method to prepare CoFe BMHs NFs, CoFe BMHs NSHs, CoFe BMHs NRs, and CoFe BMHs nano-spheres (CoFe BMHs NSPs) on the nickel foam surface. The porous structure of the nickel foam not only facilitates the transfer of substances during the reaction process but also compensates for the poor conductivity of CoFe BMHs. Through physical characterization and electrochemical testing, it was discovered that CoFe BMHs NSHs exhibit the most superior catalytic performance. CoFe BMHs NSHs demonstrated overpotentials of only 282 mV for OER at a current density of 100 mA cm⁻². Furthermore, the surface structural changes of CoFe BMHs NSHs during OER were measured by in situ Raman spectroscopy. This work provides valuable insights into enhancing catalytic activity by optimizing the morphology of catalysts.

2. Materials and Methods

2.1. Materials

Nickel foam was purchased from Kunshan Guangjiayuan Materials Co. LTD, China. Fe(NO₃)₃·9H₂O (97.5wt%) and Co(NO₃)₂·6H₂O (97.0wt%) were bought from Macklin, Shanghai, China. Urea (CH₄N₂O, 96.5wt%), NH₄F (99.5wt%), KOH (98wt%), and NaH₂PO₂ (99.0wt%) were bought from Aladdin, Shanghai, China.

2.2. Synthesis of CoFe BMHs NFs, CoFe BMHs NSHs, CoFe BMHs NRs, and CoFe BMHs NSPs

First, the nickel foams were ultrasonically cleaned with 3 M HCl for 15 min to remove the oxide layer on the surface, followed by alternating with alcohol and deionized water. For the synthesis of CoFe BMHs NFs, a Solution A was prepared by dissolving 404 mg of Fe(NO₃)₃·9H₂O, 289 mg of Co(NO₃)₂·6H₂O, 1.2 g of urea, and 370.3 mg of NH₄F in 30 mL of deionized water. For CoFe BMHs NSHs, Solution B was made with 404 mg of Fe(NO₃)₃·9H₂O, 578 mg of Co(NO₃)₂·6H₂O, 0.6 g of urea, and 370.3 mg of NH₄F in 30 mL of deionized water. Solution C for CoFe BMHs NRs was prepared by dissolving 404 mg of

$\text{Fe}(\text{NO}_3)_3 \cdot 9\text{H}_2\text{O}$, 578 mg of $\text{Co}(\text{NO}_3)_2 \cdot 6\text{H}_2\text{O}$, 1.2 g of urea, and 154.3 mg of NH_4F in 30 mL of deionized water. Lastly, Solution D for CoFe BMHs NSPs was formulated with 202 mg of $\text{Fe}(\text{NO}_3)_3 \cdot 9\text{H}_2\text{O}$, 144.5 mg of $\text{Co}(\text{NO}_3)_2 \cdot 6\text{H}_2\text{O}$, 0.6 g of urea, 154.3 mg of NH_4F , and 42.4 mg of NaH_2PO_2 in 30 mL of deionized water. Each solution was then transferred to a 50 mL reactor liner and incubated at 120°C in an oven for 8 hours. After the oven cooled naturally, the catalysts were removed, rinsed with alcohol and distilled water, dried, and set aside.

2.3. Characterization

The electrocatalyst's chemical composition was ascertained utilizing an X-ray diffractometer (XRD, SMARTLAB (9)). Examinations of the electrocatalysts' morphology, lattice diffraction, and compositional analysis were carried out with a field-emission scanning electron microscope (FESEM, SU8020) and a transmission electron microscope (TEM, JEOL JEM 2100F). The electrocatalysts' chemical composition was evaluated using X-ray photoelectron spectroscopy (XPS, Thermo Kalpha). In situ characterization of the samples was performed using HORIBA's LabRAM HR Evolution high-resolution Raman imaging spectrometer.

2.4. Electrochemical Measurements

All electrochemical data were obtained using the Kesite electrochemical workstation (CS Studio6, Wuhan Kesite Instrument Co., Ltd.). A three-electrode working system was employed for OER testing. The prepared material served as the working electrode, a platinum sheet was used as the counter electrode, and the Hg/HgO electrode was used as the reference electrode. OER performance tests were conducted in 1 M O_2 -saturated KOH solutions. The test voltage was converted to the voltage of the reversible hydrogen electrode (RHE) using the Nernst Equation ($E_{\text{RHE}} = E_{\text{Hg/HgO}} + 0.059 \text{ pH} + 0.098 \text{ V}$). For overall water splitting testing, a two-electrode working system was employed, with the prepared material serving as the anode and a platinum sheet serving as the cathode. All measurements were carried out in

an electrolytic cell containing 1 M KOH. Linear sweep voltammetry (LSV) curves were recorded at a scan rate of 5 mV s⁻¹ without iR-compensation. Tafel slopes were obtained using the equation ($\eta = a + b \log(j)$) according to LSV curves. Electrochemical impedance spectroscopy (EIS) was performed over a frequency range from 10⁶ to 10⁻² Hz. Stability tests were conducted by subjecting the catalyst to constant current polarization, and the change in catalyst activity was observed over a 30-hour testing period. The double-layer charging capacitance (C_{dl}) was obtained from the voltammetric cycle (CV) curves in the non-Faraday zone recorded at different scan rates (5, 20, 40, 60, 80, 100 mV cm⁻²), C_{dl} is proportional to the electrochemically active surface area (ECSA). The ECSA was calculated through the equation: $ECSA = C_{dl}/C_s$, where C_s represents the ideal specific capacitance of a smooth planar surface made of the same material. Here C_s was assumed to equal 0.060 mF cm⁻² [27]. The current density (j) measured is divided by the ECSA of the material to obtain j_{ECSA} ($j_{ECSA} = j/ECSA$).

3. Results and discussion

3.1 Preparation and Characterization of CoFe BMHs

The synthesis of CoFe BMHs with diverse morphologies was achieved by adjusting the ratio of Co²⁺, Fe³⁺, NH₄F, urea, and NaH₂PO₂. Urea plays a crucial role in maintaining the pH of the solution within a suitable range. Under certain temperatures, urea decomposes to produce ammonia (NH₃), which then reacts with water to form ammonium hydroxide (NH₄OH). This process can further break down into OH⁻, providing a favorable environment for the growth of bimetallic hydroxides and enhancing their yield. Additionally, fluoride ions (from NH₄F) may replace some of the OH⁻ groups in the bimetallic hydroxide structure, which can influence the overall morphology. The Co:Fe ratio and content also play a crucial role in determining the morphology of the catalyst. The Co:Fe ratios for the different CoFe BMHs samples are summarized in Table S1 (Supporting Information). Specifically, the ratios

for CoFe BMHs NFs, CoFe BMHs NSPs, CoFe BMHs NSHs, and CoFe BMHs NRs are approximately 0.70:1, 1.63:1, 1.68:1, and 0.93:1, respectively. These variations in the Co:Fe ratio create distinct growth environments for the catalyst, which in turn affect the direction and rate of crystal growth, ultimately influencing the catalyst's morphology. Additionally, we observed that the concentrations of Fe^{3+} and Co^{2+} ions significantly impact the final morphology of the samples. For example, CoFe BMHs NSPs can achieve the desired morphology even with a lower metal ion concentration compared to the other CoFe BMHs samples. Fig. 1(a) presents a schematic illustration of various CoFe BMHs morphologies on bare nickel foam (Figure S1, Supporting Information). CoFe BMHs NFs, CoFe BMHs NSHs, CoFe BMHs NRs, and CoFe BMHs NSPs make the foam nickel reddish brown, light brown, brown, and silver gray, respectively. SEM images reveal the distinct morphologies of CoFe BMHs formed on the nickel foam substrate. In Figs. 1(b) and (c), CoFe BMHs NFs exhibit a flower-like structure with a diameter of approximately $7.5 \mu\text{m}$, densely arrayed on the nickel foam surface. Figs. 1(d) and (e) show CoFe BMHs NSHs as micron-sized flakes with a thickness of 100 nm, which grow uniformly and perpendicularly in an interlocking arrangement. CoFe BMHs NRs shown in Figs. 1(f) and (g) are rod-like structures, measuring 2.5 micrometers in length, scattered across the nickel foam surface. Lastly, CoFe BMHs NSPs in Figs. 1(h) and (i) are spherical particles with a diameter of less than $8 \mu\text{m}$, sparsely distributed on the nickel foam. SEM elemental mapping analysis was conducted on the CoFe BMHs NFs, CoFe BMHs NSHs, CoFe BMHs NRs, and CoFe BMHs NSPs, and their respective energy-dispersive X-ray spectroscopy (EDS) spectra are presented in Figs. S2-5 (Supporting Information). These results demonstrate that Co and Fe elements are uniformly distributed in the synthesized BMHs. Additionally, CoFe BMHs NSHs were detached from the nickel foam for TEM examination (Fig. 1(j)). The high-resolution TEM (HRTEM) image of CoFe BMHs NSHs (Fig. 1(k)) revealed lattice fringes with spacings of 0.15 and 0.26 nm, corresponding to the (113) and (012) crystal planes of CoFe BMHs. The selected area electron diffraction (SAED) pattern (Fig. 1(l)) further confirmed the presence of these crystal planes. Elemental analysis indicated a Fe: Co ratio of approximately 1: 1.6 (Fig. S6, Supporting Information). Moreover, the EDS mapping image in Fig. 1(m) demonstrates the uniform distribution of Co, Fe, and O elements for the CoFe BMHs NSHs.

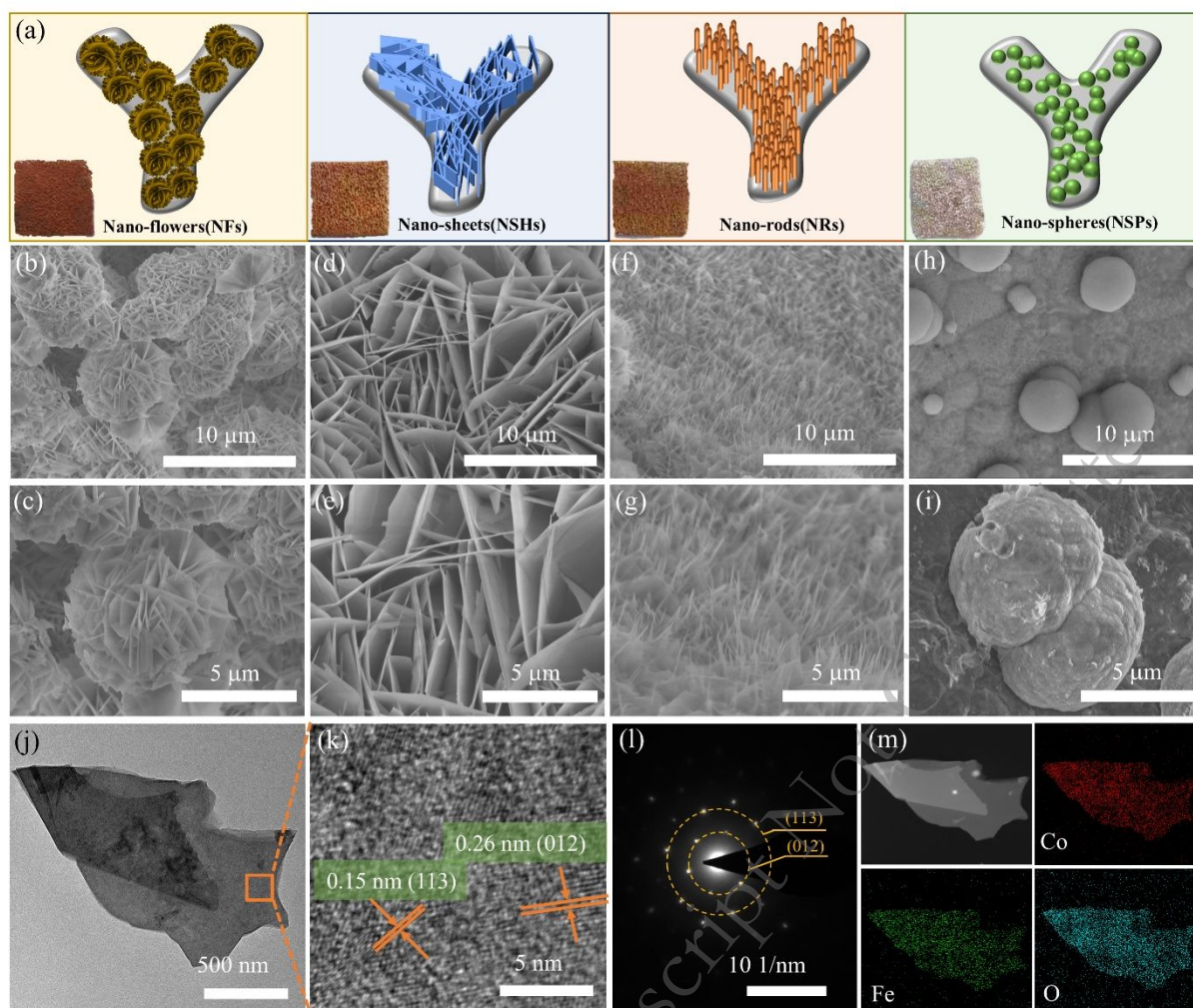


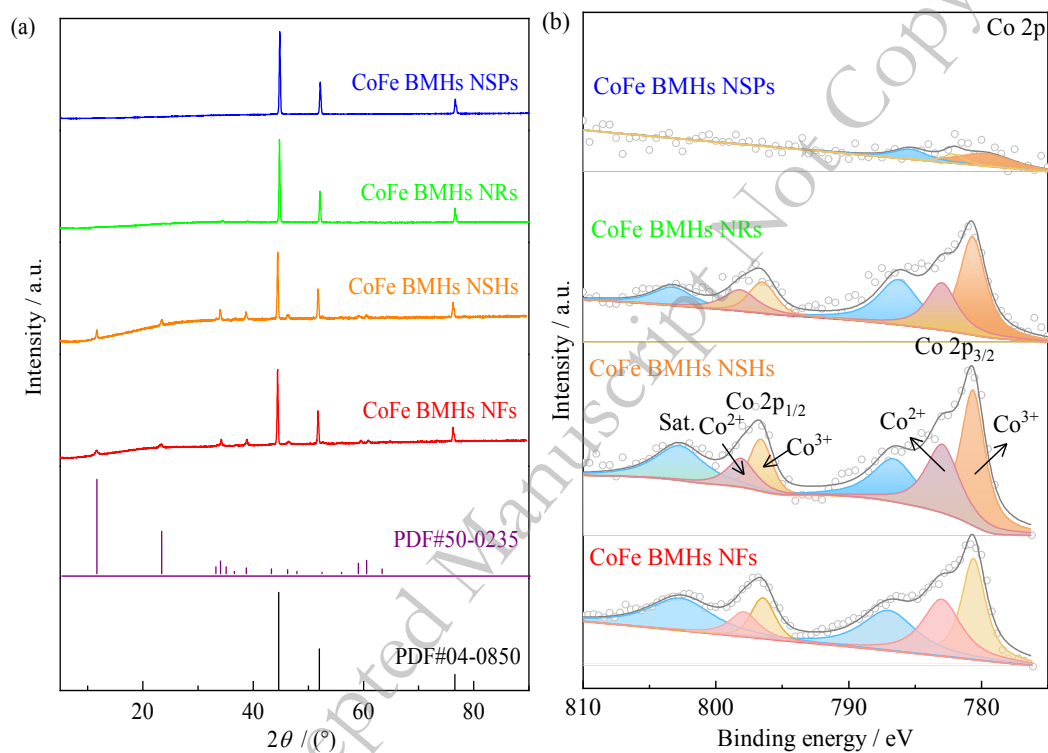
Fig. 1. (a) Illustration of different morphologies of CoFe BMHs. (b, c) SEM images of CoFe BMHs NFs. (d, e) SEM images of CoFe BMHs NSHs. (f, g) SEM images of CoFe BMHs NRs. (h, i) SEM images of CoFe BMHs NSPs. (g) TEM image of CoFe BMHs NSHs exfoliated nickel foam form and corresponding (k) HRTEM images, (l) SAED pattern, and (m) EDS mapping images.

The XRD patterns of CoFe BMHs with morphologies of NFs, NSHs, NRs, and NSPs are displayed in Fig. 2(a). The corresponding magnification of the patterns is displayed in Fig. S7. It can be observed that the three prominent peaks at 2θ values of 44.6° , 51.8° , and 76.4° correspond to the (111), (200), and (220) planes of Ni (JCPDS card No. 04-0850), respectively, which are consistent with the bare nickel foam (Fig. S8, Supporting Information). In addition, CoFe BMHs NFs, CoFe BMHs NSHs, and CoFe BMHs NRs exhibit several smaller diffraction peaks at 2θ values of 11.65° , 23.42° , 34.07° , 38.73° ,

46.23°, 59.09°, 60.54°, and 63.40°, corresponding to the (003), (006), (012), (015), (018), (110), (113), and (0113) planes of CoFe BMHs (JCPDS card No. 50-0235). This indicates the deposition of a significant amount of CoFe BMHs on the surface of the nickel foam for CoFe BMHs NFs, CoFe BMHs NSHs, and CoFe BMHs NSPs. However, no additional CoFe BMHs diffraction peaks are observed for CoFe BMHs NSPs. This is because CoFe BMHs NSPs grow sparsely and are dispersed on the nickel foam, resulting in a larger exposed surface area of the bare nickel foam.

Furthermore, the surface chemical composition and oxidation states of the compounds were examined utilizing XPS. The XPS survey spectra depicted in Fig. S9 reveal the presence of Co, Fe, and O in the catalysts, in concordance with the findings from EDS. In Fig. 2(b), the Co 2p_{3/2} and Co 2p_{1/2} spin-orbit doublet peaks, along with the shake-up satellite peaks, form a four-peak spectrum. For CoFe BMHs NSHs, a deconvolution analysis was performed on the Co 2p_{3/2} and Co 2p_{1/2} peaks to distinguish between the different oxidation states. The peaks at 780.5 and 796.5 eV correspond to Co³⁺ [28], while those at 782.9 and 798.1 eV correspond to Co²⁺ [29-30]. The peaks at 786.6 and 802.9 eV are associated with satellite peaks [31-32]. The positions of the Co 2p peaks for CoFe BMHs NFs and CoFe BMHs NRs are largely consistent with those of CoFe BMHs NSHs. Due to the lower loading amount, the Co 2p_{1/2} peak in CoFe BMHs NSPs is less distinct. For CoFe BMHs NSHs, the Fe 2p spectrum was fitted with two sets of peaks, corresponding to Fe 2p_{3/2} and Fe 2p_{1/2} at 712.6 and 725.2 eV [33], and two satellite peaks at 717.9 and 732.5 eV [34-35], respectively (Fig. 2(c)). In comparison, the Fe 2p spectra of CoFe BMHs NFs, NRs, and NSPs also exhibit similar peak positions. Fig. 2(d) shows the peaks of O1s, with the various O species overlapping each other

as seen from the XPS spectra. The peaks from left to right are assigned to surface adsorbed oxygen (H_2O), hydroxide ($-\text{OH}$) [36], and metal-oxygen (M-O) species [22, 37] in CoFe BMHs, respectively. Metal-oxygen (M-O) is the main active species in the OER process [38]. The weakening of the relative peak intensity of M-O in CoFe BMHs NSPs compared to CoFe BMHs NFs, CoFe BMHs NSHs, and CoFe BMHs NRs indicates a decrease in the content of the active species, which is in agreement with the results of the high-resolution spectra of Co 2p versus Fe 2p.



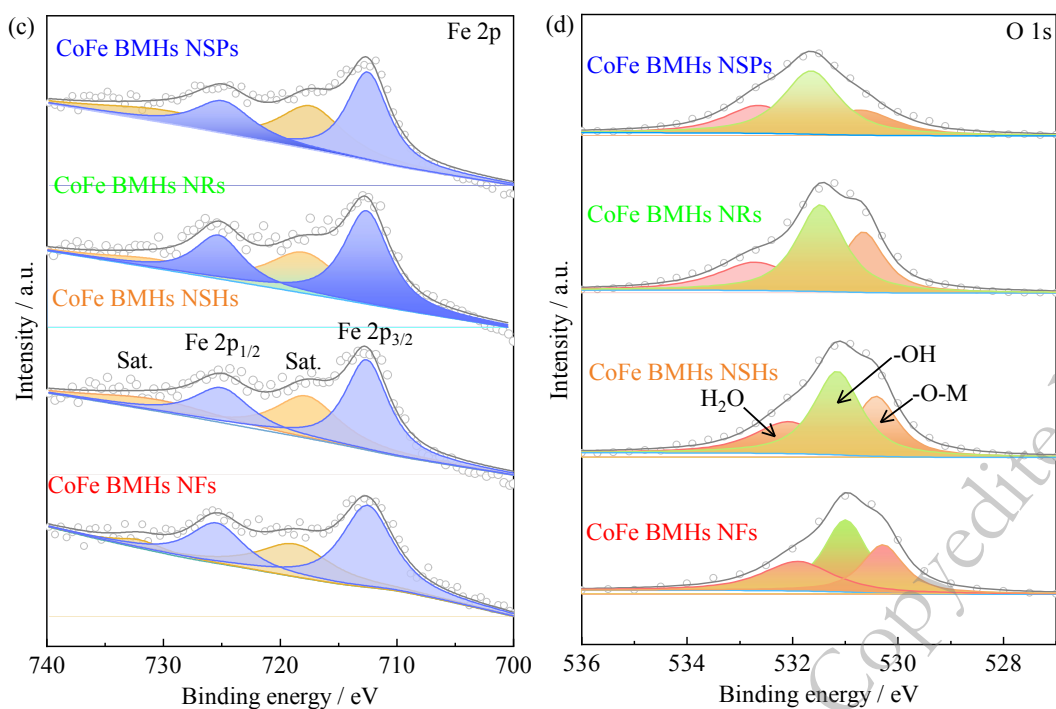
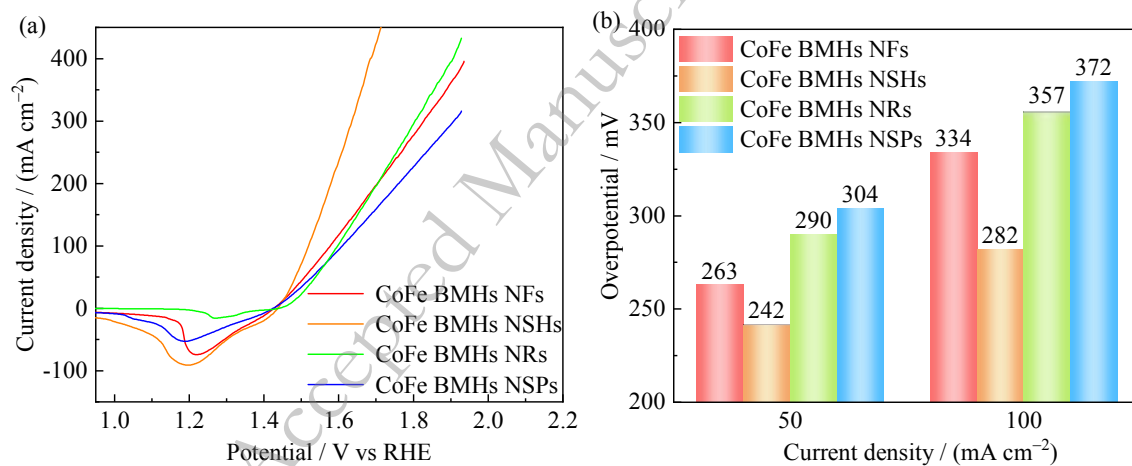


Fig. 2. (a) XRD patterns of CoFe BMHs NFs, CoFe BMHs NSHs, CoFe BMHs NRs, and CoFe BMHs NSPs. Comparison XPS spectra of (b) Co 2p, (c) Fe 2p, and (d) O 1s for different catalysts.

3.2. OER Performances of CoFe BMHs

The electrochemical test results for OER are presented in Fig. 3. Fig. 3(a) displays the LSV test results for all CoFe BMHs catalysts. To eliminate the influence of the oxidation peaks of Co^{2+} and Fe^{2+} in the catalysts, a negative scan was performed for all CoFe BMHs. From the graph, it can be observed that at a current density of 10 mA cm^{-2} , the overpotentials for CoFe BMHs NFs, CoFe BMHs NSHs, CoFe BMHs NRs, and CoFe BMHs NSPs are 208, 212, 233, and 215 mV, respectively. As the current density increases to 50 mA cm^{-2} , the overpotentials are 263, 242, 290, and 304 mV, respectively. Further increasing the current density to 100 mA cm^{-2} , the overpotentials are 334, 282, 357, and 372 mV Fig. 3(b), respectively. CoFe BMHs NSHs exhibit lower overpotential compared to other catalysts, indicating superior OER performance of CoFe BMHs NSHs. The Tafel slopes of the catalysts are presented in Fig. 3(c). The values for CoFe BMHs NFs, CoFe BMHs NSHs, CoFe BMHs

NRs, and CoFe BMHs NSPs are 150.9, 133.5, 156.1, and 151.4 mV dec^{-1} , respectively. CoFe BMHs NSHs exhibit the smallest Tafel slope, indicating the fastest reaction rate and highest catalytic activity, which is consistent with the LSV test results. EIS spectra of the catalysts are shown in Fig. 3(d). It can be observed that the R_{ct} values for CoFe BMHs NFs, CoFe BMHs NSHs, CoFe BMHs NRs, and CoFe BMHs NSPs are 0.65, 0.30, 0.88, and 1.35 Ω (Table S2, Supporting Information), respectively. CoFe BMHs NSHs have the smallest R_{ct} , indicating the least hindrance to charge transfer in the circuit and the highest energy conversion and transmission efficiency. The above electrochemical measurements indicate that CoFe BMHs NSHs exhibit excellent OER performance. Besides, our CoFe BMHs demonstrate clear advantages over the CoFe hydroxides/LDHs reported in the literature (Table S3, Supporting Information).



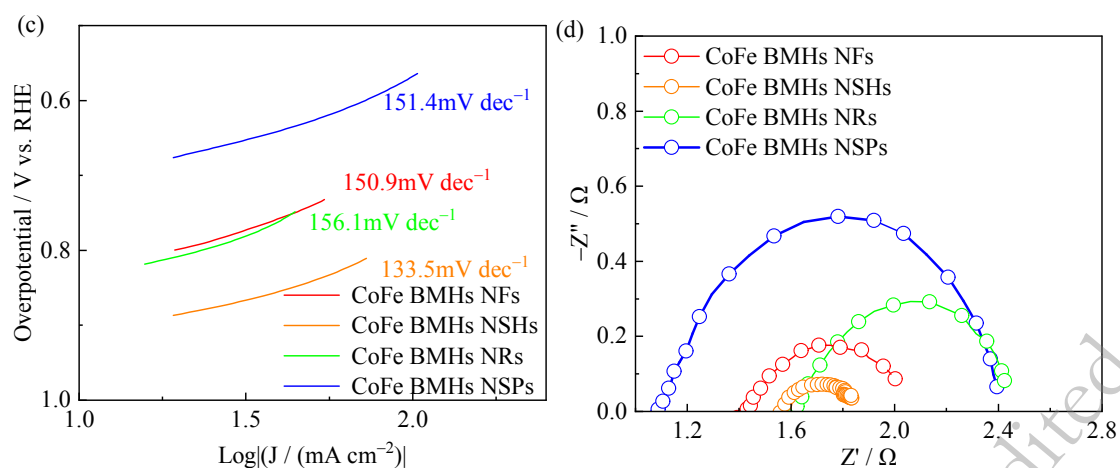


Fig. 3. OER was measured in 1 M KOH solution saturated with O_2 . (a) LSV curves, (b) overpotentials at 50 and 100 $mA\ cm^{-2}$, (c) Tafel plots, (d) EIS plot of CoFe BMHs NFs, CoFe BMHs NSHs, CoFe BMHs NRs, and CoFe BMHs NSPs, respectively.

3.3 Analysis of Excellent Performance of CoFe BMHs NSHs

To further investigate the reasons for the superior performance of CoFe BMHs, the ECSA of the catalysts was measured. The C_{dl} values of CoFe BMHs NFs, CoFe BMHs NSHs, CoFe BMHs NRs, and CoFe BMHs NSPs were calculated based on the CV curves in the appropriate potential range (0.924-1.024 V vs. RHE) (Figs. 4(a-d)), which are 3.28, 1.42, 1.22, and 1.14 $mF\ cm^{-2}$, respectively (Fig. 4(e)). The higher the C_{dl} value, the larger the ECSA. The ECSA values for CoFe BMHs NFs, CoFe BMHs NSHs, CoFe BMHs NRs, and CoFe BMHs NSPs are 54.66, 23.66, 20.33, and 19.00, respectively. The high ECSA value of CoFe BMHs NSHs is evidence that they possess the largest active area in the OER process. To clarify the source of this enhanced activity, the specific activity represented by the current density normalized by ECSA was compared. As shown in Fig. 4(f), CoFe BMHs NFs, CoFe BMHs NSHs, and CoFe BMHs NSPs exhibit similar specific activity, indicating that the increased current density of CoFe BMHs NSHs is mainly due to the higher exposure of active sites. CoFe BMHs NRs, compared to CoFe BMHs NFs, CoFe BMHs NSHs, and CoFe BMHs

NSPs, show a higher j_{ECSA} at voltages greater than 1.62 V (vs. RHE), suggesting that CoFe BMHs NRs have stronger intrinsic activity at voltages above 1.62 V (vs. RHE). This finding is crucial in establishing their potential as efficient catalysts for overall water splitting.

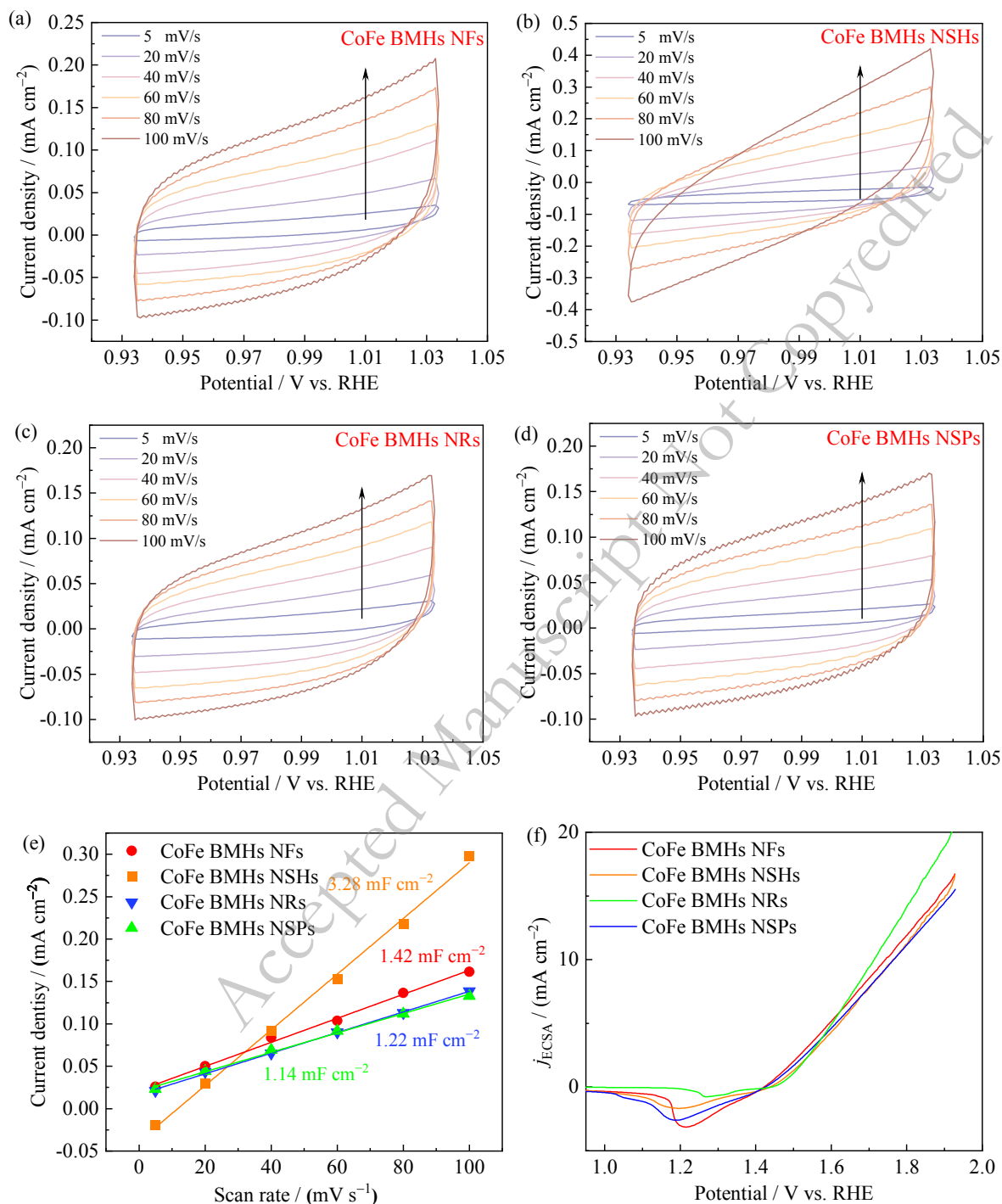


Fig. 4. (a) CV curves (0.925-1.025 V vs RHE) of (a) CoFe BMHs NFs, (b) CoFe BMHs NSHs, (c) CoFe BMHs NRs, and (d) CoFe BMHs NSPs at various scan rate for OER. (e) C_{dl} plot. (f) LSV curves with current density normalized by ECSA.

The surface structural changes of CoFe BMHs NSHs during OER in 1.0 M KOH solution were measured by in situ Raman. In the in situ cell, the polarization curves can be simulated by the continuous chronopotentiometry (CP) method by first increasing the potential from 1.2 V to 1.55 V and then decreasing the potential to 1.2 V. The reaction was carried out for a certain period at each potential to obtain the Raman spectra. Figs. 5(a) and (b) shows the in situ Raman spectra and corresponding contour plots of CoFe BMHs NSHs, respectively. As can be seen in Fig. 5(a), the Raman peak of CoFe BMHs NSHs is not significant without voltage application. After the start of voltage application, in the wave number range of 200-600 cm^{-1} , the sample shows BMHs signal at 317 cm^{-1} , which corresponds to the E-type vibration [39-40]. Correspondingly, two Raman peaks appear at 468 and 574 cm^{-1} corresponding to the bending vibration of E_g ($\delta(\text{M-O})$) and the stretching vibration of A_{1g} ($\nu(\text{M-O})$) of the MOOH [20, 41-43]. The width and wave number of the $\delta(\text{M-O})$ and $\nu(\text{M-O})$ peaks gradually increase with increasing voltage applied intensity. It indicates that more MOOH species are produced at higher voltages [44]. The observed phase transition was found to be irreversible upon the voltage reduction back to 1.2 V, indicating that the active species for the OER is likely the surface MOOH, rather than the MOH. Intermediates adsorbed on the catalyst surface were also detected. Weakly absorbed nitrate is shown at 1060 cm^{-1} . NO_3^- is necessary to balance the additional cation charge in the layered CoFe BMHs NSHs. At 1.45 V, all peaks associated with NO_3^- fade away, implying that desorption of NO_3^- is a prerequisite for the complete conversion of MOH to MOOH [44]. In the spectral range 1100-1200 cm^{-1} , the peak corresponding to 1150 cm^{-1} is the broad band of $\nu(\text{O-O})$ of reactive oxygen species, which is produced by deprotonation of hydroxyl oxides, suggesting the production of O_2 [45].

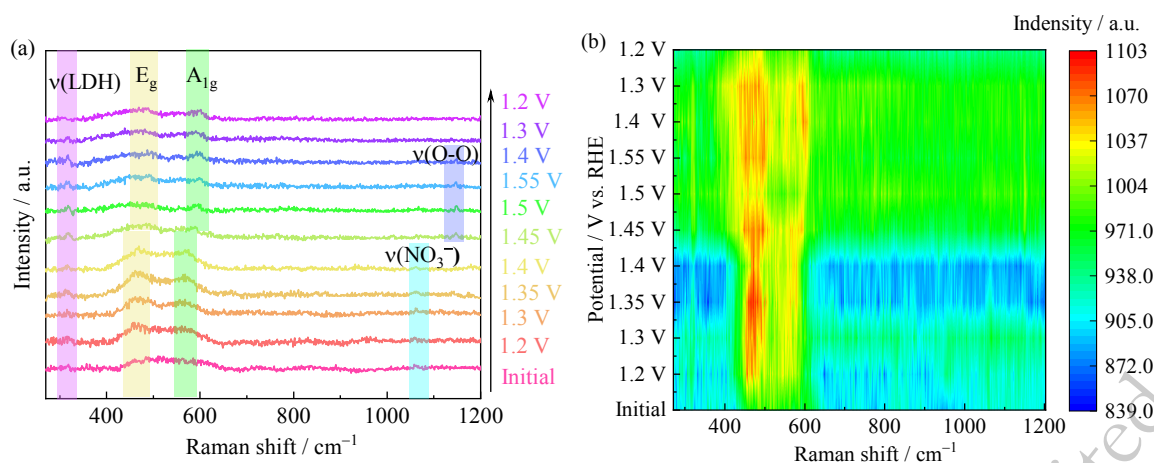


Fig. 5. (a) In situ Raman spectra of CoFe BMHs NSHs. (b) Corresponding contour plots of the Raman spectra.

3.4. Overall Water Splitting Performance

In the process of water splitting using a dual-electrode cell, the catalysts are used as the anode of the electrolyzer, and the platinum sheet is used as the cathode of the electrolyzer. The electrochemical test results for overall water splitting are presented in Fig. 6. As shown in Fig. 6(a), CoFe BMHs NSHs achieve a current density of 10 mA cm^{-2} at a voltage of only 1.503 V, while CoFe BMHs NFs, CoFe BMHs NRs, and CoFe BMHs NSPs require voltages of 1.530, 1.644, and 1.579 V, respectively. At a current density of 100 mA cm^{-2} , the voltages are 1.962, 1.923, 2.004, and 2.021V, respectively (Fig. 6(b)). CoFe BMHs NSHs demonstrate the lowest electrolysis voltage, indicating superior performance. The stability test results for overall water splitting using CoFe BMHs NSHs are presented in Fig. 6(c). The electrocatalytic efficiency of the catalyst is over 98% at a current density of 50 mA cm^{-2} for 30 hours, demonstrating its excellent stability. Additionally, SEM characterization of the reacted catalyst was done (Fig. S10). The SEM results indicated that the catalyst retained its morphology after the reaction, suggesting that no collapse occurred during the phase transition. We further performed XRD characterization on the catalyst before and after the

reaction (Fig. S11). The results reveal a shift in peak positions, indicating that a partial transition from MOH to MOOH occurred during the reaction process. This observation is consistent with our in situ Raman results. It indicates that the overall crystal structure remains largely intact and only subtle changes occur at the molecular or bonding level, resulting in peak shifts rather than the emergence of new peaks or the disappearance of existing ones. A photograph of the electrolytic cell during the stability test using CoFe BMHs NSHs is shown in Fig. 6(d), where continuous bubbles were generated on the surfaces of the cathodic and anodic catalysts, corresponding to H₂ and O₂ evolution, respectively. These tests demonstrate the promising application prospects of CoFe BMHs NSHs in the field of hydrogen production via water splitting.

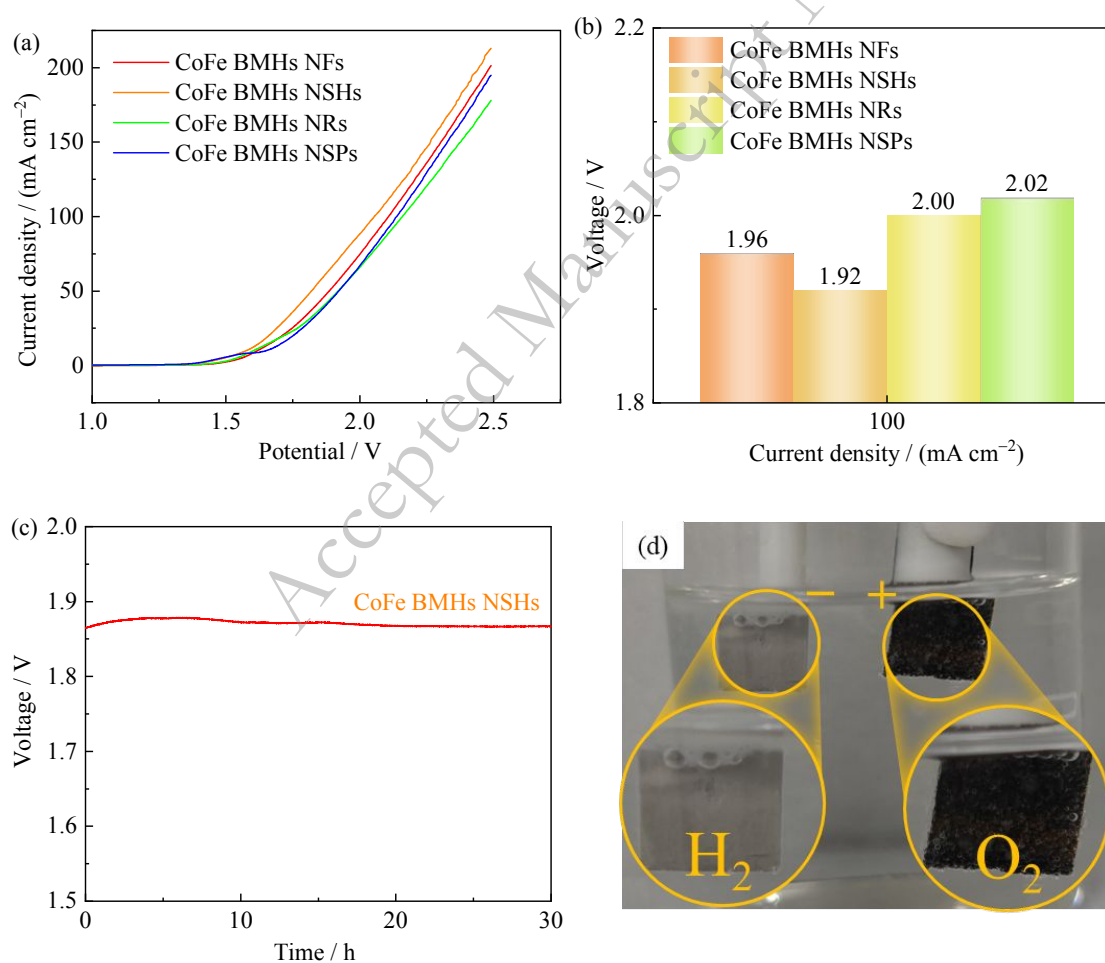


Fig. 6. Overall water splitting was measured in 1 M KOH solution. (a) LSV curves and (b)

Potential of different electrocatalysts at 100 mA cm⁻². (c) Stability test curve of CoFe BMHs NSHs. (d) Optical photograph of H₂ and O₂ produced by CoFe BMHs NSHs as cathode and anode of electrolytic cell.

4. Conclusions

In this study, CoFe BMHs NFs, CoFe BMHs NSHs, CoFe BMHs NRs, and CoFe BMHs NSPs were synthesized using a hydrothermal method. Through investigations of their morphology, composition, and electrochemical performance, it was found that CoFe BMHs NSHs exhibited the best performance in terms of OER and overall water splitting. At a current density of 100 mA cm⁻², CoFe BMHs NSHs demonstrated overpotentials of 282 mV for OER and a voltage of 1.923 V for overall water splitting. Furthermore, the in situ Raman test revealed the process of physical phase change during the OER reaction, verifying that the active substance of OER is mainly MOOH. These findings highlight the significant influence of different morphologies of the same material on catalytic performance and provide design insights for catalysts in other complex systems.

Acknowledgements

L.M. Yang and Y.B. Cao contributed equally to this work. This work was supported by the National Science Fund for Distinguished Young Scholars (NO. 52025041), the National Natural Science Foundation of China (NO. 52474319, 52250091, U2341267, 52450003), the Fundamental Research Funds for the Central Universities of NO. FRF-TP-20-02C2. This project is supported by the Interdisciplinary Research Project for Young Teachers of USTB (Fundamental Research Funds for the Central Universities) (NO. FRF-IDRY-GD23-003).

References

- [1] X.Y. Jie, S. Gonzalez-Cortes, T.C. Xiao, B.Z. Yao, J.L. Wang, D.R. Slocombe, Y.W. Fang, N. Miller, H.A. Al-Megren, J.R. Dilworth, J.M. Thomas, and P.P. Edwards, The decarbonisation of petroleum and other fossil hydrocarbon fuels for the facile production and safe storage of hydrogen, *Energy Environ. Sci.*, 12(2019), No. 1, p. 238.
- [2] X. Zeng, Y. Ye, Y. Wang, R. Yu, M. Moskovits and G. D. Stucky, Honeycomb-like MXene/NiFePx-NC with "continuous" single-crystal enabling high activity and robust

- durability in electrocatalytic oxygen evolution reactions, *J. Adv. Ceram.*, 12(2023), No.3, p. 553.
- [3] X. Zhao, X.W. Ma, B.Y. Chen, Y.P. Shang, and M.L. Song, Challenges toward carbon neutrality in China: Strategies and countermeasures, *Resour. Conserv. Recycl.*, 176(2022), No., p. 105959.
- [4] X.J. Lin, S.F. Cao, X.D. Chen, H.Y. Chen, Z.J. Wang, H.H. Liu, H. Xu, S.Y. Liu, S.X. Wei, and X.Q. Lu, Two birds with one stone: contemporaneously boosting OER activity and kinetics for layered double hydroxide inspired by photosystem II, *Adv. Funct. Mater.*, 32(2022), No. 27, p. 2202072.
- [5] X.X. Ji, Y.H. Lin, J. Zeng, Z.H. Ren, Z.J. Lin, Y.B. Mu, Y.J. Qiu, and J. Yu, Graphene/MoS₂/FeCoNi(OH)_x and Graphene/MoS₂/FeCoNiP_x multilayer-stacked vertical nanosheets on carbon fibers for highly efficient overall water splitting, *Nat. Commun.*, 12(2021), No. 1, p. 1380.
- [6] F. Dai, Z. Wang, H. Xu, C. Jiang, Y. Ouyang, C. Lu, Y. Jing, S. Yao, and X. Wei, Metal-organic framework derived NiFe₂O₄/FeNi₃@C composite for efficient electrocatalytic oxygen evolution reaction, *Int. J. Min. Met. Mater.*, 30(2023), No. 10, p. 1914.
- [7] L. Zeng, Z. Zhao, F. Lv, Z. Xia, S.Y. Lu, J. Li, K. Sun, K. Wang, Y. Sun, Q. Huang, Y. Chen, Q. Zhang, L. Gu, G. Lu, and S. Guo, Anti-dissolution Pt single site with Pt(OH)(O₃)/Co(P) coordination for efficient alkaline water splitting electrolyzer, *Nat. Commun.*, 13(2022), No. 1, p. 3822.
- [8] Y. Qin, T. Yu, S. Deng, X.Y. Zhou, D. Lin, Q. Zhang, Z. Jin, D. Zhang, Y.B. He, H.J. Qiu, L. He, F. Kang, K. Li, and T.Y. Zhang, RuO₂ electronic structure and lattice strain dual engineering for enhanced acidic oxygen evolution reaction performance, *Nat. Commun.*, 13(2022), No. 1, p. 3784.
- [9] Y.X. Zhao, Q.L. Wen, D.J. Huang, C. Jiao, Y.W. Liu, Y. Liu, J.K. Fang, M. Sun, and L. Yu, Operando reconstruction toward dual-cation-defects Co-containing NiFe oxyhydroxide for ultralow energy consumption industrial water splitting electrolyzer, *Adv. Energy Mater.*, 13(2023), No. 10, p. 2203595.
- [10] D. Li, C.J. Zhou, R. Yang, Y.Y. Xing, S.J. Xu, D.L. Jiang, D. Tian, and W.D. Shi, Interfacial engineering of the Co_xP–Fe₂P heterostructure for efficient and robust electrochemical overall water splitting, *ACS Sustain. Chem. Eng.*, 9(2021), No. 23, p. 7737.
- [11] H.B. Ma, Z.W. Chen, Z.L. Wang, C.V. Singh, and Q. Jiang, Interface engineering of Co/CoMoN/NF heterostructures for high-performance electrochemical overall water splitting, *Adv. Sci.*, 9(2022), No. 11, p. 2105313.
- [12] Y. Zhang, H.R. Guo, X.P. Li, J. Du, W.L. Ren, and R. Song, A 3D multi-interface structure of coral-like Fe-Mo-S/Ni₃S₂@NF using for high-efficiency and stable overall water splitting, *Chem. Eng. J.*, 404(2021), No., p. 126483.
- [13] X.Y. Zhao, K.W. Tang, X.M. Wang, W.H. Qi, H. Yu, C.-F. Du, and Q. Ye, A self-supported bifunctional MoNi₄ framework with iron doping for ultra-efficient water splitting, *J. Mater. Chem. A.*, 11(2023), No. 7, p. 3408.
- [14] Q. Huang, Y. Yang, and J. Qian, Structure-directed growth and morphology of multifunctional metal-organic frameworks, *Coordin. Chem. Rev.*, 484(2023), p. 215101.
- [15] Z. Chen, K. Huang, B. Zhang, J. Xia, J. Wu, Z. Zhang, and Y. Huang, Corrosion

- engineering on AlCoCrFeNi high-entropy alloys toward highly efficient electrocatalysts for the oxygen evolution of alkaline seawater, *Int. J. Min. Met. Mater.*, 30(2023), No. 10, p. 1922.
- [16] W. N. Yang, J. Li, M.Y. Wang, X.F. Sun, Y. Liu, J. Yang, and D. H. L. Ng, A colorimetric strategy for ascorbic acid sensing based on the peroxidase-like activity of core-shell Fe₃O₄/CoFe-LDH hybrid, *Colloid Surf. B-Biointerfaces*, 188(2020), No., p. 110742.
- [17] B. Yang, Y. Wu, X.P. Li, and R.H. Yu, Surface-oxidized FeCo/carbon nanotubes nanorods for lightweight and efficient microwave absorbers, *Mater. Des.*, 136(2017), No. 15, p. 13.
- [18] X.Q. Han, Z.H. Lin, X.Q. He, L.L. Cui, and D.X. Lu, The construction of defective FeCo-LDHs by in-situ polyaniline curved strategy as a desirable bifunctional electrocatalyst for OER and HER, *Int. J. Hydrog. Energy*, 45(2020), No. 51, p. 26989.
- [19] Z.C. Li, X.Y. Wang, J.W. Ren, and H. Wang, NiFe LDH/Ti₃C₂T_x/nickel foam as a binder-free electrode with enhanced oxygen evolution reaction performance, *Int. J. Hydrog. Energy*, 47(2022), No. 6, p. 3886.
- [20] J. Han, H. Wang, Y. Wang, H. Zhang, J. Li, Y. Xia, J. Zhou, Z. Wang, M. Luo, Y. Wang, N. Wang, E. Cortés, Z. Wang, A. Vomiero, Z.-F. Huang, H. Ren, X. Yuan, S. Chen, D. Feng, X. Sun, Y. Liu and H. Liang, Lattice Oxygen Activation through Deep Oxidation of Co₄N by Jahn–Teller–Active Dopants for Improved Electrocatalytic Oxygen Evolution, *Angew. Chem. Int. Edit.*, 63(2024), No.33, p. e202405839.
- [21] X. Guo, M.G. Li, L.Y. Qiu, F.Y. Tian, L. He, S. Geng, Y.Q. Liu, Y. Song, W.W. Yang, and Y.S. Yu, Engineering electron redistribution of bimetallic phosphates with CeO₂ enables high-performance overall water splitting, *Chem. Eng. J.*, 453(2023), No. 1, p. 139796.
- [22] S. Wang, F. Yuan, G.X. Yang, S.C. Luo, M. Chen, T.T. Fan, and J.T. Ma, In situ construction of CoFe-LDH by regulating the Co/Fe molar ratio for promoting oxygen evolution reaction, *Mol. Catal.*, 525(2022), No., p. 112339.
- [23] L.Y. Hu, L.Y. Tian, X. Ding, X. Wang, X.S. Wang, Y. Qin, W.L. Gu, L. Shi, and C.Z. Zhu, p–d hybridization in CoFe LDH nanoflowers for efficient oxygen evolution electrocatalysis, *Inorg. Chem. Front.*, 9(2022), No. 20, p. 5296.
- [24] H. Feng, X. Sun, X. Guan, D.C. Zheng, W.L. Tian, C.Y. Li, M.L. Yan, and Y.D. Yao, Construction of interfacial engineering on CoP nanowire arrays with CoFe-LDH nanosheets for enhanced oxygen evolution reaction, *FlatChem*, 26(2021), No., p. 100225.
- [25] C.Y. Hao, Y.Wu, Y.J. An, B.H. Cui, J.N. Lin, X.N. Li, D.H. Wang, M.H. Jiang, Z.X. Cheng, and S. Hu, Interface-coupling of CoFe-LDH on MXene as high-performance oxygen evolution catalyst, *Mater. Today Energy*, 12(2019), No., p. 453.
- [26] B. Deng, J. Liang, L.C. Yue, T.S. Li, Q. Liu, Y. Liu, S.Y. Gao, A.A. Alshehri, K.A. Alzahrani, Y. Luo, and X.P. Sun, CoFe-LDH nanowire arrays on graphite felt: A high-performance oxygen evolution electrocatalyst in alkaline media, *Chin. Chem. Lett.*, 33(2022), No. 2, p. 890.
- [27] Y. Yao, G. Zhao, X. Guo, P. Xiong, Z. Xu, L. Zhang, C. Chen, C. Xu, T.-S. Wu, Y.-L. Soo, Z. Cui, M. M.-J. Li and Y. Zhu, Facet-Dependent Surface Restructuring on Nickel (Oxy)hydroxides: A Self-Activation Process for Enhanced Oxygen Evolution Reaction, *J. Am. Chem. Soc.*, 146(2024), No.22, p. 15219.

- [28] Y. P. Li, J. D. Liu, C. Chen, X. Zhang and J. Chen, Preparation of NiCoP hollow quasi-polyhedra and their electrocatalytic properties for hydrogen evolution in alkaline solution, *ACS Appl. Mater. Interfaces*, 9(2017), No. 7, p. 5982.
- [29] H. Wu, J. Wang, J. Yan, Z. Wu and W. Jin, MOF-derived two-dimensional N-doped carbon nanosheets coupled with Co-Fe-P-Se as efficient bifunctional OER/ORR catalysts, *Nanoscale*, 11(2019), No. 42, p. 20144.
- [30] L. Liu, N. Li, J. Han, K. Yao and H. Liang, Multicomponent transition metal phosphide for oxygen evolution, *Int. J. Min. Met. Mater.*, 29(2022), No. 3, p. 503.
- [31] M. P. Chen, D. Liu, B. Y. Zi, Y. Y. Chen, D. Liu, X. Y. Du, F. F. Li, P. F. Zhou, Y. Ke, J. L. Li, K. H. Lo, C. T. Kwok, W. F. Ip, S. Chen, S. P. Wang, Q. J. Liu and H. Pan, Remarkable synergistic effect in cobalt-iron nitride/alloy nanosheets for robust electrochemical water splitting, *J. Energy Chem.*, 65(2022), No., p. 405.
- [32] L. Y. Hu, M. Y. Li, X. Q. Wei, H. J. Wang, Y. Wu, J. Wen, W. L. Gu and C. Z. Zhu, Modulating interfacial electronic structure of CoNi LDH nanosheets with Ti_3C_2T MXene for enhancing water oxidation catalysis, *Chem. Eng. J.*, 398(2020), No., p. 125605.
- [33] P. Aggarwal, B. Singh and A. Paul, Pore size and electronic tuning in cerium-doped CoFe-LDH for the oxygen evolution reaction, *Mater. Adv.*, 4(2023), No. 19, p. 4377.
- [34] Y. Deng, J. Wang, S.-F. Zhang, Z.-J. Zhang, J.-F. Sun, T.-T. Li, J.-L. Kang, H. Liu and S. Bai, In situ constructing lamella-heterostructured nanoporous CoFe/CoFe₂O₄ and CeO_{2-x} as bifunctional electrocatalyst for high-current-density water splitting, *Rare Metals*, (2024).
- [35] S. Shankar Naik, J. Theerthagiri, F. S. Nogueira, S. J. Lee, A. Min, G.-A. Kim, G. Maia, L. M. C. Pinto and M. Y. Choi, Dual-cation-coordinated CoFe-layered double-hydroxide nanosheets using the pulsed laser ablation technique for efficient electrochemical water splitting: mechanistic screening by in situ/operando Raman and density functional theory calculations, *ACS Catal.*, 13(2023), No. 2, p. 1477.
- [36] W. Yan, J. Zhang, A. Lü, S. Lu, Y. Zhong and M. Wang, Self-supporting and hierarchically porous Ni_xFe—S/NiFe₂O₄ heterostructure as a bifunctional electrocatalyst for fluctuating overall water splitting, *Int. J. Min. Met. Mater.*, 29(2022), No. 5, p. 1120.
- [37] C. B. Wei, C. Liu, L. N. Gao, Y. F. Sun, Q. Y. Liu, X. Zhang and J. X. Guo, MoS₂ nanosheets decorated Ni(OH)₂ nanorod array for active overall water splitting, *J. Alloy. Compd.*, 796(2019), No. 5, p. 86.
- [38] J. X. Han, X. Y. Meng, L. Lu, J. J. Bian, Z. P. Li and C. W. Sun, Single-atom Fe-N_x-C as an efficient electrocatalyst for Zinc-air batteries, *Adv. Funct. Mater.*, 29(2019), No. 41, p. 1808872.
- [39] K. Luo, M. R. Roberts, R. Hao, N. Guerrini, D. M. Pickup, Y.-S. Liu, K. Edström, J. H. Guo, A. V. Chadwick and L. C. Duda, Charge-compensation in 3 d-transition-metal-oxide intercalation cathodes through the generation of localized electron holes on oxygen, *Nat. Chem.*, 8(2016), No. 7, p. 684.
- [40] J.-L. Bantignies, S. Deabate, A. Righi, S. Rols, P. Hermet, J.-L. Sauvajol and F. Henn, New insight into the vibrational behavior of nickel hydroxide and oxyhydroxide using inelastic neutron scattering, far/mid-infrared and Raman spectroscopies, *J. Phys. Chem. C*, 112(2008), No. 6, p. 2193.
- [41] X. Bo, Y.B. Li, X.J. Chen, and C.A. Zhao, Operando Raman spectroscopy reveals Cr-induced-phase reconstruction of NiFe and CoFe oxyhydroxides for enhanced

- electrocatalytic water oxidation, *Chem. Mat.*, 32(2020), No. 10, p. 4303.
- [42] C. Wang, P.L. Zhai, M.Y. Xia, W. Liu, J.F. Gao, L.C. Sun, and J. G. Hou, Identification of the origin for reconstructed active sites on oxyhydroxide for oxygen evolution reaction, *Adv. Mater.*, 35(2023), No. 6, p. 2209307.
- [43] Q. Li, Q. Chen, K. Jiang, S.F. Lei, Y.L. Deng, and J. Bao, Boosting high-current water electrolysis: Superhydrophilic/superaerophobic nanosheet arrays of NiFe LDH with oxygen vacancies in situ grown on iron foam, *Int. J. Hydrog. Energy*, 48(2023), No. 46, p. 17501.
- [44] H. Sun, L. Chen, Y. Lian, W. Yang, L. Lin, Y. Chen, J. Xu, D. Wang, X. Yang, M.H. Rümmerli, J. Guo, J. Zhong, Z. Deng, Y. Jiao, Y. Peng, and S. Qiao, Topotactically transformed polygonal mesopores on ternary layered double hydroxides exposing under-coordinated metal centers for accelerated water dissociation, *Adv. Mater.*, 32(2020), No. 52, p. 2006784.
- [45] Y.F. Hu, C.J. Hu, A.X. Du, T.T. Xiao, L.F. Yu, C.K. Yang, and W. Xie, Interfacial evolution on Co-based oxygen evolution reaction electrocatalysts probed by using in situ surface-enhanced Raman spectroscopy, *Anal. Chem.*, 95(2023), No. 2, p. 1703.

Accepted Manuscript Not Certified